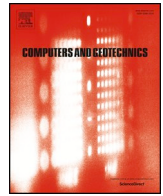




ELSEVIER

Contents lists available at ScienceDirect

## Computers and Geotechnics

journal homepage: [www.elsevier.com/locate/compgeo](http://www.elsevier.com/locate/compgeo)

Research Paper

## Interaction between granular flows and flexible obstacles: A grain-scale investigation

C.E. Choi<sup>a,b</sup>, G.R. Goodwin<sup>b,\*</sup><sup>a</sup> The University of Hong Kong Shenzhen Institute of Research and Innovation, Nanshan, Shenzhen, China<sup>b</sup> Department of Civil Engineering, The University of Hong Kong, Pokfulam, Hong Kong Special Administrative Region

## ARTICLE INFO

## Keywords:

Landslides  
Flexible barriers  
Grain intruder  
Landslide mitigation

## ABSTRACT

Flexible obstacles are used to reduce the impact load exerted by granular flows. However, grain-scale interactions between granular assemblies and flexible obstacles remain poorly understood, making it difficult to estimate the required resisting force. In this fundamental study, a flexible obstacle was simplified as a grain intruder and dragged through a static granular assembly. A new physical intruder apparatus was used to calibrate a discrete element model. The calibrated model was then used to evaluate the effects of the stiffness and loading rate on the force experienced by the intruder and the energy dissipated by the granular assembly. The response of the intruder and the granular assembly depended significantly on both the drag rate and the obstacle stiffness. Softer obstacles caused longer sticks between slips. At least 60% of the work was transferred from the intruder into the granular assembly regardless of the drag rate and obstacle stiffness. Stick-slip behaviour was not observed for stiff obstacles and high drag rates ( $> 1$  m/s), where the bulk granular assembly fluidised. The results of this study suggest that rigid obstacles are better for causing energy dissipation in the granular assembly, while flexible obstacles are better for reducing the resisting forces required.

## 1. Background

The impact of granular flows on rigid obstacles has been widely studied (e.g. Faug et al., 2002, 2009; Moriguchi et al., 2009; Teufelsbauer et al., 2011; Sano & Hayakawa, 2012; Faug, 2015; Albaba et al., 2018; Ceccato et al., 2018; Lee et al., 2019; Goodwin & Choi, 2020; Leonardi & Pirulli, 2020). However, the fundamental mechanisms whereby flexible barriers and obstacles resist granular flows are relatively unclear. Studies such as those of Wendeler et al. (2007), Brighenti et al. (2013), Ashwood & Hungr (2016), Ng et al. (2016), Albaba et al. (2017) and Song et al. (2019a) focused mainly on the macroscopic responses of flexible structures impacted by granular flows. It has been reported that flexible barriers may absorb as little as 8% of the flow energy (Song et al., 2019a). A possible explanation for this is that granular flows are efficient at dissipating kinetic energy through internal processes such as frictional shearing (Mitarai & Nakanishi, 2007). However, the relationships among the obstacle stiffness, loading rate, and energy dissipation, as well as the fundamental mechanisms whereby energy is dissipated, remain poorly understood. Improvements to the design of flexible resisting structures, which is currently empirical (GEO, 2014), hinge on an improved understanding of this relationship.

At the mesoscopic scale and low shear rates, energy-dissipation processes for dense granular flows can occur as part of a two-stage cyclic process known as ‘stick-slip’ (e.g. Johnson et al., 2008; Tordesillas et al., 2014). First, there is a progressive increase in the bulk stress in the material. The bulk stress is distributed through a force-chain network (Muthuswamy & Tordesillas, 2006). Second, at a critical point, a sudden displacement occurs, buckling the force-chain network and causing stress release and redistribution (Tordesillas et al., 2014). These stress redistributions can cause energy dissipation through both frictional shearing and inelastic collisions.

In previous studies on stick-slip, a ‘grain-intruder’ setup was adopted (e.g. Albert et al., 1999, 2000, 2001; Geng & Behringer, 2005; Candelier & Dauchot, 2009, 2010; Harich et al., 2011; Hilton & Tordesillas, 2013; Kolb et al., 2013; Tordesillas et al., 2014). In grain-intruder experiments, a body is pulled through a granular mass using a spring. The spring can be either physical or virtual. (The latter is applicable to computational simulations.) Grain intruders can serve either as (i) intrusive measuring devices that provide insight into the bulk material strength and the manner in which the bulk granular assembly rearranges during interactions or (ii) obstacles that an assembly of grains move around, as viewed from a Lagrangian frame of reference. The latter perspective on grain intruders is helpful for gaining a

\* Corresponding author.

E-mail addresses: [cechoi@hku.hk](mailto:cechoi@hku.hk) (C.E. Choi), [cegeorge@hku.hk](mailto:cegeorge@hku.hk) (G.R. Goodwin).

fundamental understanding of grain-scale interactions between granular flows and obstacles under relatively uniform “flow” conditions. The grain-intruder approach neglects certain aspects of granular flows, specifically (i) the shear and granular temperature profiles and hence (ii) the energy dissipation due to interlayer shearing and grain collisions. However, granular flows are typically spilt into shear and plug layers (Iverson, 1997). The shear and granular temperatures within the rigid plug region of a granular flow are limited. As such, the results of the grain-intruder approach are relevant to the interaction between the plug layer and an obstacle.

Albert et al. (1999, 2000) investigated a columnar intruder being dragged through a granular assembly. They found that the drag force depends on the cylinder diameter and depth of insertion but not the drag rate. They also reported that the contact area between the intruder and the assembly did not affect the stick-slip behaviour. The drag rate in both studies was on the order of mm/s. In the latter study, the spring constant was varied over the range of 0.5–10 kN/m. Geng and Behringer (2005) used a two-dimensional annular setup to study the movement of a disk through a granular array at velocities on the order of mm/s, finding that drag force fluctuations were associated with the formation and destruction of force chains. Tordesillas et al. (2014) dragged a single particle at 10 mm/s using a spring with a stiffness of  $k = 1$  kN/m through an assembly of grains. The evolution of the force-chain network during the shearing was examined.

There are gaps in the knowledge obtained from these studies related to (i) the effects of the stiffness on the impact force and (ii) mobilising the granular assembly so that it can dissipate energy. Furthermore, the aforementioned studies were conducted at low shear rates. For dynamic problems, such as flow-type landslides, high shear rates occur. Because granular flows in the field can have a wide range of impact velocities, it is important to consider both the stick-slip and fluidised regimes comprehensively. Addressing this gap is crucial for gaining a fundamental understanding of the response of flexible obstacles impacted by flows travelling at different rates.

In this study, a physical grain-intruder apparatus was used to understand the fundamental behaviour of a flexible obstacle. The experimental results were used to calibrate a discrete element model. The calibrated model was then used to conduct a parametric study to examine the spring stiffness  $k$  ( $0.1 < k < 100$  kN/m) over a range of drag rates ( $0.25 < U < 32$  m/s), where the spring stiffness represents the obstacle stiffness.

## 2. Methodology

### 2.1. Physical test

A physical experiment was performed using a new intruder apparatus (Fig. 1a and b). The purpose of the experiment was to generate data for evaluating the discrete element model setup and input parameters. The intruder apparatus consisted of two compartments. The main compartment holding the granular assembly had dimensions of 1.0 m by 0.2 m by 0.5 m (length  $\times$  width  $\times$  height). At one end of the box, there was a separate compartment to house a pulley system. A wire with a diameter of 2 mm was threaded between the compartments. A single grain with a diameter of 25 mm was attached at the end of the wire in the main box. In the smaller compartment, a pulley led the wire to a tensile load cell, which was connected to a pneumatic piston. When the piston retracted, the grain intruder was dragged through the granular assembly.

The box was filled with glass spheres with a diameter of 25 mm up to the height of the ball attached to the wire (Fig. 1c(i)). The intruder was then placed on top of the inserted spheres near the far end of the box (Fig. 1c(ii)). The rest of the spheres were then inserted into the storage compartment to provide an overburden of 2.1 kPa (Fig. 1c(iii)). The “flow” material was modelled as an initially static array of grains. As such, the average bulk density was likely higher than that of an

equivalent prototype flow. This corresponds to the “plug layer” of a flow, i.e. a region with limited internal shearing that sits atop a “shear layer” (Iverson, 1997).

After the sample was prepared, the instrumentation was activated, and the pneumatic piston was set to the desired force, dragging the grain intruder through the sample (Fig. 1c(iv)) at an average velocity of 1 m/s. For the calibration simulation using the discrete element method (DEM), this setup was exactly replicated, and rigid planes were used to model the sidewalls and base. An oblique schematic is shown in Fig. 1d; the initial ( $x, y, z$ ) coordinates of the centroid of the grain intruder were (0.1, 0.1, 0.1), as measured from the far end of the intruder setup, for both the physical tests and the DEM calibration simulation.

### 2.2. Discrete element method

In this study, the open-source version of the DEM software LIGGGHTS (Kloss and Goniva, 2011) was adopted. In the DEM, the forces acting on each grain at each timestep are calculated:

$$m_i \frac{dv_i}{dt} = F + m_i g, \quad (1)$$

where  $m_i$  represents the mass of each grain,  $v_i$  represents the velocity of each grain,  $t$  represents time,  $F$  represents the non-gravitational external forces acting on the grain, and  $g$  represents the gravitational acceleration. The position of each grain can be evaluated using Newton’s equations of motion. When grains come into contact with each other, the external force  $F$  can be split into normal and tangential components  $F_n$  and  $F_t$ :

$$F = F_n + F_t = (k_n d_{nij} - \gamma_n v_{nij}) + (k_t d_{tij} - \gamma_t v_{tij}), \quad (2)$$

where  $k_n$  and  $k_t$  represent the particle spring stiffnesses, which vary depending on the elastic moduli  $E$ , the shear moduli  $G$ , the grain radii  $r$ , and the penetration distance  $d$ . (Note: the particle spring stiffnesses are a material property, and are not the same as the virtual spring stiffness investigated parametrically in this paper.) The parameters  $\gamma_n$  and  $\gamma_t$  are functions of the coefficient of restitution  $e$ , as well as  $E$ ,  $G$ ,  $r$ ,  $d$ , and  $m$ . The parameters used in this study have previously been evaluated against various experiments involving granular flows (e.g. Ng et al., 2019; Goodwin & Choi, 2020). Their values, which are presented in Table 1, agreed with the physically observed flow kinematics in small-scale experiments using flows of glass spheres.

#### 2.2.1. Numerical domain for DEM parametric study

The DEM grain-intruder setup for the parametric study included a computational domain with a length and width of  $20\delta$  and a finite depth (Fig. 2). The length and width of  $20\delta$  were sufficient to prevent the bulk granular assembly from interacting with itself unrealistically across periodic boundaries. A single rigid plane was generated in the  $xy$ -plane to form the base of the container. Periodic boundaries were applied in the  $xz$ - and  $yz$ - planes to simulate an infinitely large container.

#### 2.2.2. Numerical procedure

The numerical procedure was essentially identical for both the calibration simulation and the parametric study. The only differences were (i) the shape and boundaries of the numerical domain; (ii) the position where the grain intruder was generated; and (iii) the confining stress on the intruder. The dimensions of the box for the calibration simulation were 1.0 m  $\times$  0.2 m  $\times$  0.5 m, with non-periodic boundaries. For the parametric study, the dimensions of the simulation domain were  $20\delta$  m  $\times$   $20\delta$  m  $\times$  1 m. The intruder was generated at  $x, y$ , and  $z$  coordinates of (0.1, 0.1, 0.1) m for the calibration simulation and ( $2\delta$ ,  $10\delta$ , 0.1) m for the parametric study. The confining stress was 2.1 kPa for the calibration simulation and 8.0 kPa for the parametric study.

For both the calibration simulation and the parametric study, the intruder was first generated at the appropriate location. The bulk

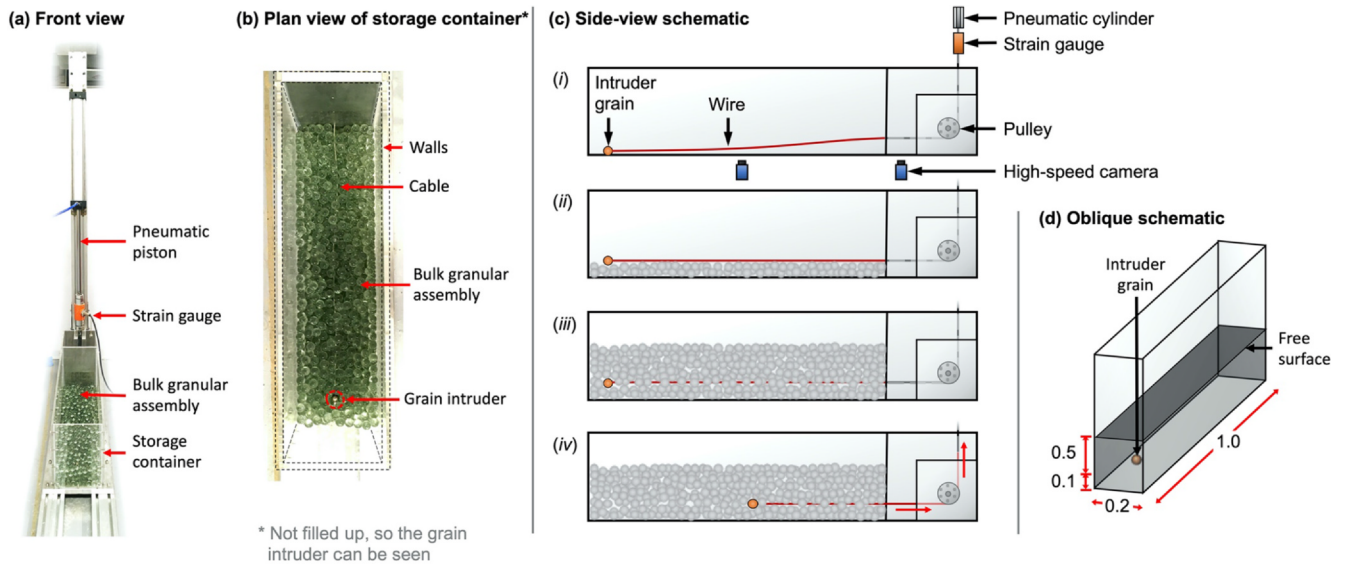


**Fig. 1.** (a) Frontal view of the physical intruder apparatus; (b) plan view of the physical intruder storage container; (c) side-view schematic of granular material being placed into physical intruder – (i) to (iii) – and then the grain intruder being dragged (iv); (d) oblique schematic of the physical experiment and the DEM model for the calibration.

**Table 1**  
Parameters adopted in numerical simulations.

	DEM simulations
Diameter (m)	0.010 ± 0.001
Material density (kg/m <sup>3</sup> )	2650
Internal friction angle (°)	19.8
Interface friction angle (°)	16.6
Young's modulus (Pa)	10 <sup>8</sup>
Poisson's ratio	0.3
Rolling resistance	0
Contact model	Hertzian
Coefficient of restitution	0.5

granular assembly was then generated and allowed to settle. For both cases, the grain size for the granular assembly was nominally identical to that of the grain intruder, although a slight degree of polydispersity (± 10%) was applied to reduce the crystallisation effects (Tordesillas

et al., 2014; Marchelli et al., 2019). For the calibration simulation, the vertical height above the grain was 0.13 m, resulting in a confining stress of 2.1 kPa. In the parametric study, the vertical height above the grain was 0.51 m, corresponding to a normal confining stress of 8 kPa. There was a total of ~7500 grains per simulation in the parametric study.

For both the calibration simulation and the parametric study, a virtual spring was fixed to one end of the grain intruder (see Fig. 2b). (The combination of the virtual spring and the intruder represent an obstacle with a given flexibility.) The free end of the virtual spring was initially tethered to the centroid of the grain intruder and was then pulled away at a constant velocity. The mobilised tension  $T$  in the spring varied according to the following equation:

$$T = k(x_{\text{spring}} - x_{\text{intruder}}), \tag{3}$$

where  $k$  represents the spring constant,  $x_{\text{spring}}$  represents the position of the tether point of the spring being dragged (see Fig. 2b), and  $x_{\text{intruder}}$

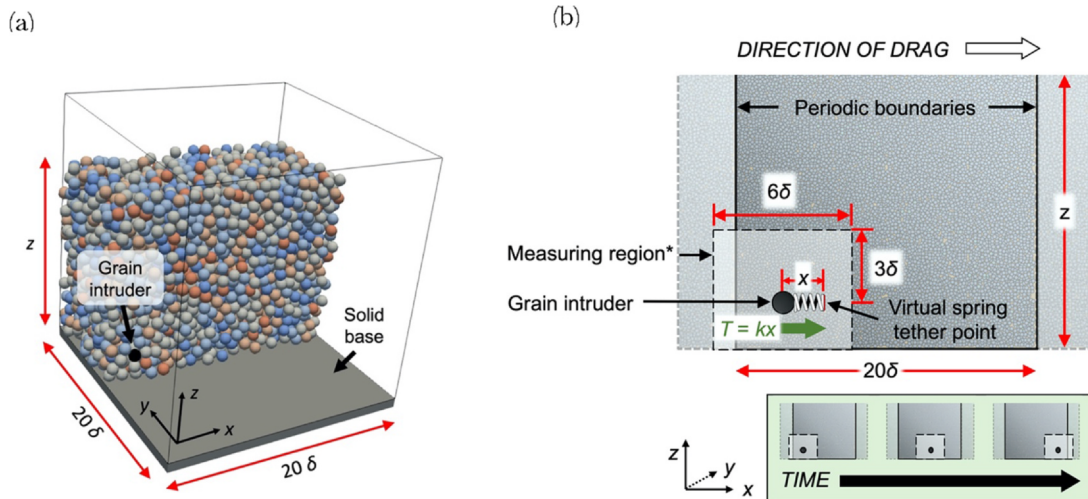


**Fig. 2.** (a) Configuration of system, with half of the grains of one side cut away. Colouring indicates grain radii. (b) Side-view schematic of the system (not to scale). The green box shows qualitatively how the system evolves over time. \* The measuring region is three-dimensional, with a side in the y-direction of  $6\delta$ , and follows the grain intruder as it moves through the computational domain. The measuring region is used only to extract the solid volume fraction and grain Froude number; all other quantities presented apply either to just the grain intruder or the entire granular assembly.

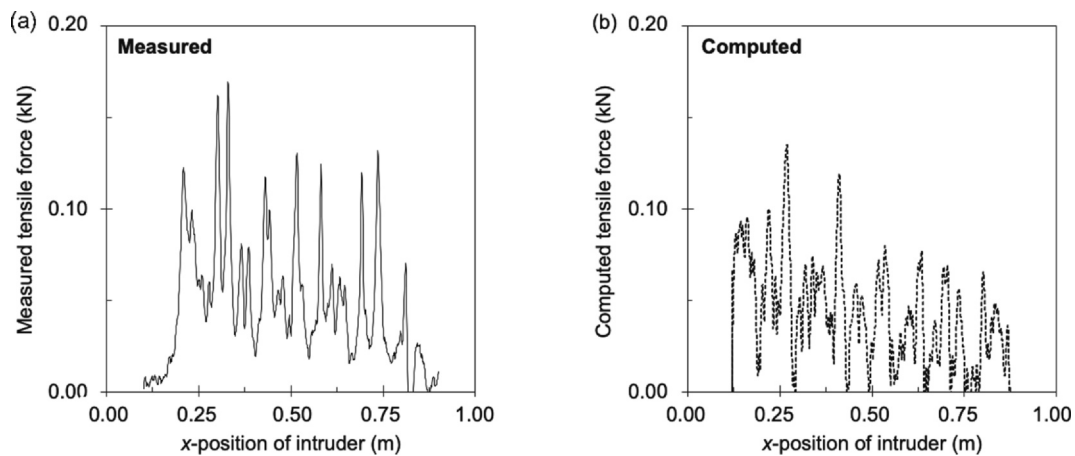


Fig. 3. (a) Measured tensile force from the physical intruder experiment; (b) computed tensile force from the DEM calibration. For both cases, the overburden was 2.1 kPa; the drag speed was 1 m/s; and the grain size was 25 mm. The spring stiffness for the virtual spring in the DEM was set to 20 kN/m.

represents the centroid of the grain intruder. The calibration simulation was terminated when the grain intruder reached  $x = 0.9$  m. For the parametric study simulations,  $x = 18\delta$  was adopted as the threshold for terminating the simulation.

### 2.2.3. Calibration of discrete element model using physical test

A comparison of the measured tensile forces for the physical experiment and numerical simulation is presented in Fig. 3a and b. For both the physical experiment and the numerical simulation, the overburden was approximately 2.1 kPa, the drag rate was 1 m/s, and the grain sizes of both the grain intruder and the bulk assembly were 25 mm. The stiffness of the virtual spring in the numerical calibration simulation was set as 20 kN/m. As shown in Fig. 3, the numerical model captured the essential characteristics of the physical experiment. There were several relatively large force peaks that corresponded to the grain intruder becoming stuck, although the force peaks were slightly smaller in the DEM tests. The magnitude of these peaks decreased as the intruder moved across the domain because of a segregation effect that occurs for relatively low confining stresses (see Ding et al., 2011). This segregation effect was not observed in the other numerical tests in the present study, where a larger confining stress was adopted. The comparison results confirm the ability of the discrete element model to capture the essential physics of the problem.

### 2.3. Test variables

The drag rate and spring stiffness were varied, where the spring stiffness represents the obstacle stiffness. The input parameters for the simulations were selected to be relevant to prototype debris flows. Drag rates of 0.25–32 m/s were chosen to cover the typical range of speeds of debris flows, which can reach approximately 30 m/s (Rickenmann, 1999). The overburden was selected according to the depth of prototype flows reported by Iverson (1997); for instance, the 1982 Oddstad debris flow had a depth of 1 m. Because the grain-intruder setup is most relevant to the plug region of the flow, an overburden of 0.5 m was selected. The eight drag rates and four spring stiffnesses considered provided a total of 32 distinct cases (Table 2). Each of the 32 simulation

cases was repeated 20 times with different pseudo-randomly generated arrangements of the bulk granular assembly. The quantities presented in the interpretation of the results were the averages across these sets (Figs. 8 and 9).

The range of stiffnesses of the virtual spring was selected with consideration of the wide range of barrier stiffnesses adopted in previous studies and engineering applications. Canelli et al. (2012) performed small-scale flume tests, modelling a flexible barrier made of chicken-wire with an aperture of 1.5 cm. Although an equivalent stiffness for the barrier was not given, it is assumed to have a similar magnitude to that of the chicken-wire used by Huo et al. (2017), i.e. 0.45 kN/m. Koo et al. (2016) modelled the dynamic response of flexible rockfall barriers using a finite-element method (FEM) package capable of simulating large deformations. The net barrier was modelled as an array of interlocking rings based on a commercially available product (Rocco 7/3/300 net rings). The elastic material modulus of the rings was set as 200 GPa, and the elastic modulus of the wire rope cables was set as 100 GPa. Leonardi et al. (2016) used a coupled computational fluid dynamics–DEM approach to model a two-phase flow interacting with a flexible barrier. They analysed a range of equivalent stiffnesses of the net ranging from 0.15 to 40 GPa. Song et al. (2019b) performed simulations modelling the spring-element stiffness range of 100–16000 kN/m.

In the parametric component of the present study, the stiffness range of 0.1–100 kN/m was used. Increasing the stiffness of the virtual spring beyond 100 kN/m had a negligible effect on the flow dynamics (as shown in Fig. 7a). Thus, 100 kN/m was selected as the upper bound, which is lower than the stiffnesses of certain flexible barrier elements that are commercially available and used for practical landslide mitigation.

### 3. Force-chain characterisation

Force chains are the fundamental vectors whereby load is transferred between grains and have been widely investigated in the field of geomechanics (e.g. Cates et al., 1998; Makse et al., 2000; Majmudar & Behringer, 2005; Peters et al., 2005; Tordesillas et al., 2010; Walker et al., 2017). Dragging a grain intruder through the granular assembly disrupts the force-chain network. Thus, the force-chain network is relevant for understanding the fundamental interaction mechanisms between the intruder and the bulk granular assembly.

A simple algorithm was developed for extracting information related to the strong force-chain network in contact with the grain intruder. Every  $n$  timesteps, the identification numbers of each grain (hereafter 'IDs'), the  $x$ -,  $y$ -, and  $z$ -coordinates of each grain, and the  $x$ -,  $y$ -, and  $z$ -components of the contact stresses between the grains were

Table 2  
Test program for parametric study.

Drag rate $v_{\text{drag}}$ (m/s)	Spring stiffness $k$ (kN/m)
0.25, 0.5, 1, 2, 4, 8, 16, 32	0.1
	1
	10
	100

recorded. In accordance with the method of Tordesillas et al. (2014), the contacts were filtered following the criterion  $\sigma_c > 0.5 \sigma_{\text{mean}(C)}$ ; thus, the “strong” contacts were retained. Then, the algorithm searched for grains in the bulk assembly in contact with the intruder. In cases of multiple contacts, one was picked at random. The algorithm then searched for a third grain in contact with the second. The angle formed between each pair of contacts was calculated as the dot product of the two contact vectors. If the angle was  $> 45^\circ$ , the contacts were not considered part of the chain (Peters et al., 2005; Muthuswamy and Tordesillas, 2006; Tordesillas, 2007; Tordesillas and Muthuswamy, 2009; Tordesillas et al., 2009; Tordesillas et al., 2014). The threshold of  $45^\circ$  represents the middle ground between  $0^\circ$  and  $90^\circ$ . A threshold of  $0^\circ$  would only allow perfectly linear force chains to be found (Peters et al., 2005). A threshold of  $90^\circ$  would cause all grains in physical contact in the granular assembly to be considered part of the same force chain. For a given threshold, increasing the friction angle of the granular material tends to increase the length of the force chains. This length increase is accompanied by an increase in the bulk strength of the material.

The process of searching for grains in each chain was repeated until the end of the chain was reached, at which point the IDs and stresses of the grains participating in each force chain were recorded. Then, the ID to search for was reset to that of the grain intruder, and the search for grains in contact was restarted. The whole process was looped  $q$  times, where  $q$  represents a counter. The number of unique chains was checked after each loop  $q$ . ‘Unique chains’ were determined by comparing the IDs of all of the grains participating in each chain. If the same string of IDs occurred more than once during the looping, duplicates were not counted as being unique. Once the number of loops  $q$  exceeded five times the number of unique chains  $M$  (i.e.  $q > 5M$ ), it was assumed that all the chains had been found at that timestep. The process of looping was then terminated.

After the unique force chains had been identified, the number and average length of the force chains for the timestep were recorded. The total contact stress in the  $x$ -direction was calculated for each pair of contacts in the network. The entire workflow is shown in Fig. 4a, which also contains an inset showing a two-dimensional idealisation of possible force chain configurations. Fig. 4b presents an idealised schematic of just the grains exerting a force on the intruder directly, as well as the resolved contact forces. Fig. 4c shows a schematic of the grains in the strong force-chain network, along with the resolved contact forces.

Fig. 5 shows an example of the grain intruder moving across the computational domain. The thick lines show the strong force-chain network. Other force chains are shown in light grey. At the start of the simulation (Fig. 5i), there were strong force chains both in front of and behind the grain intruder, because it was effectively part of the static bulk granular assembly. After the grain started moving (Fig. 5ii and 5iii), strong force chains mostly existed in front of the grain intruder (see also Tordesillas et al., 2014).

## 4. Results

### 4.1. Time and displacement histories: effects of spring stiffness and drag rate

Fig. 6 shows effects of dragging the grain intruder with variations in the spring stiffness and drag rate, where spring stiffness represents obstacle stiffness. Three representative cases were selected: (i)  $v_{\text{drag}} = 0.25$  m/s and  $k = 1$  kN/m; (ii)  $v_{\text{drag}} = 0.25$  m/s and  $k = 100$  kN/m; and (iii)  $v_{\text{drag}} = 32$  m/s and  $k = 1$  kN/m. The effects observed for the final case were qualitatively identical among the different spring stiffnesses. Thus, only the results for one spring stiffness are shown.

Fig. 6a(i) shows the relationship between the tensile force in the spring and the  $x$ -position of the intruder over time. The tensile force in the spring was the product of the spring constant  $k$  and the distance between the centroid of the grain intruder and the tether point  $x$ , i.e.  $T = kx$ . For this low spring stiffness and drag rate, the tensile force initially increased linearly as the assembly was loaded. When the

mobilised tensile force was sufficiently large to overcome the resistance due to the confining stress, the intruder slipped, reducing the mobilised tensile force. Subsequently, the tensile force remained relatively constant, with a mean value of approximately 0.4 kN, as the intruder underwent relatively long cycles of stick and slip. Fig. 6a(ii) shows the same drag rate but for a significantly stiffer spring. The initial increase in the tensile force was linear, but the critical tension for causing movement was reached sooner. The tension cycles exhibited a similar mean value to the previous case but at a higher frequency. The stick–slip behaviour for the intruder was less apparent because the intruder generally moved close to the tether point of the spring. The time required for the intruder to reach the end of the simulation box was approximately half of that for  $k = 1$  kN/m. As shown in Fig. 6a(iii), when the drag rate was 32 m/s, the tensile force increased rapidly and nonlinearly (similar to the behaviour of a strain hardening material). The grain intruder did not clearly exhibit stick–slip behaviour, because of the constant increase in the mobilised tensile force. These results are unique: they are fundamentally different from those of small-scale tests using smaller grain sizes and barriers that did not allow the bulk granular assembly to pass (i.e. impervious barriers). Additionally, this study differed from studies such as that of Ashwood and Hungr (2016), where dry sand flows impacting impervious rigid and flexible barriers were modelled.

Fig. 6b(i), 6b(ii), and 6b(iii) each show three data series, all as a function of the displacement. Fig. 6b(i) shows the tension. Fig. 6b(ii) shows the force on the intruder. Fig. 6b(iii) shows the total force in the strong force-chain network in the  $x$ -direction. The tension  $T$  in the virtual spring is defined as  $T = kx$ . The “force on the intruder”  $F_{\text{intr}}$  is the sum of the vector contact forces from other grains within the granular assembly that are directly acting on the grain intruder  $F_{\text{con}(i)}$  in the  $x$ -direction:

$$F_{\text{intr}} = \sum_{i=1}^{N_{\text{con}}} F_{\text{con}(i)}, \quad (4)$$

where  $i$  represents the index of grains in contact with the intruder; and  $N_{\text{con}}$  represents the number of contacts with the grain intruder. The “total force in the strong force-chain network”  $F_{\text{SF}}$  is the sum of the forces acting on each grain in the  $x$ -direction (indexed by  $i$ ) that appear in each chain in contact with the grain intruder (indexed by  $p$ ) and denoted by the symbol  $F_{\text{ch}(i,p)}$ :

$$F_{\text{SF}} = \sum_{p=1}^{N_{\text{ch}}} \sum_{i=1}^{N_{\text{con}}} F_{\text{con}(i,p)}. \quad (5)$$

Here  $p$  indexes the force chains, and  $N_{\text{ch}}$  represents the number of force chains. All three graphs indicate that regardless of the spring stiffness and drag rate, increasing the tension generally increased the reaction force in the strong force-chain network.

Additionally, Fig. 6b(i) shows that for a low drag rate and a flexible spring, the force on the grain intruder was only a small proportion of the tensile force. This implies that most of the tensile force was transferred to the bulk granular assembly. Both the reaction force and collisions with grains in the bulk assembly contributed to this force. As shown in Fig. 6b(ii), in the case where the spring was significantly stiffer, the force on the intruder was negligible. This is because the intruder underwent rapid stick–slip; thus, its velocity remained very low (and hence its impact force remained weak).

Dragging the intruder at a far higher rate (Fig. 6b(iii)) caused the force in the bulk granular assembly to change rapidly. In addition to a reaction force to the spring tension in the strong force-chain network, there was a dynamic force on grains as they rearranged in response to the grain intruder. The force on the grain intruder was proportionately higher than that in the low-strain-rate cases, owing to the dynamic loading.

Fig. 6c(i), 6c(ii), and 6c(iii) show the quantity of short and long chains in the strong force-chain network with respect to the strain. The

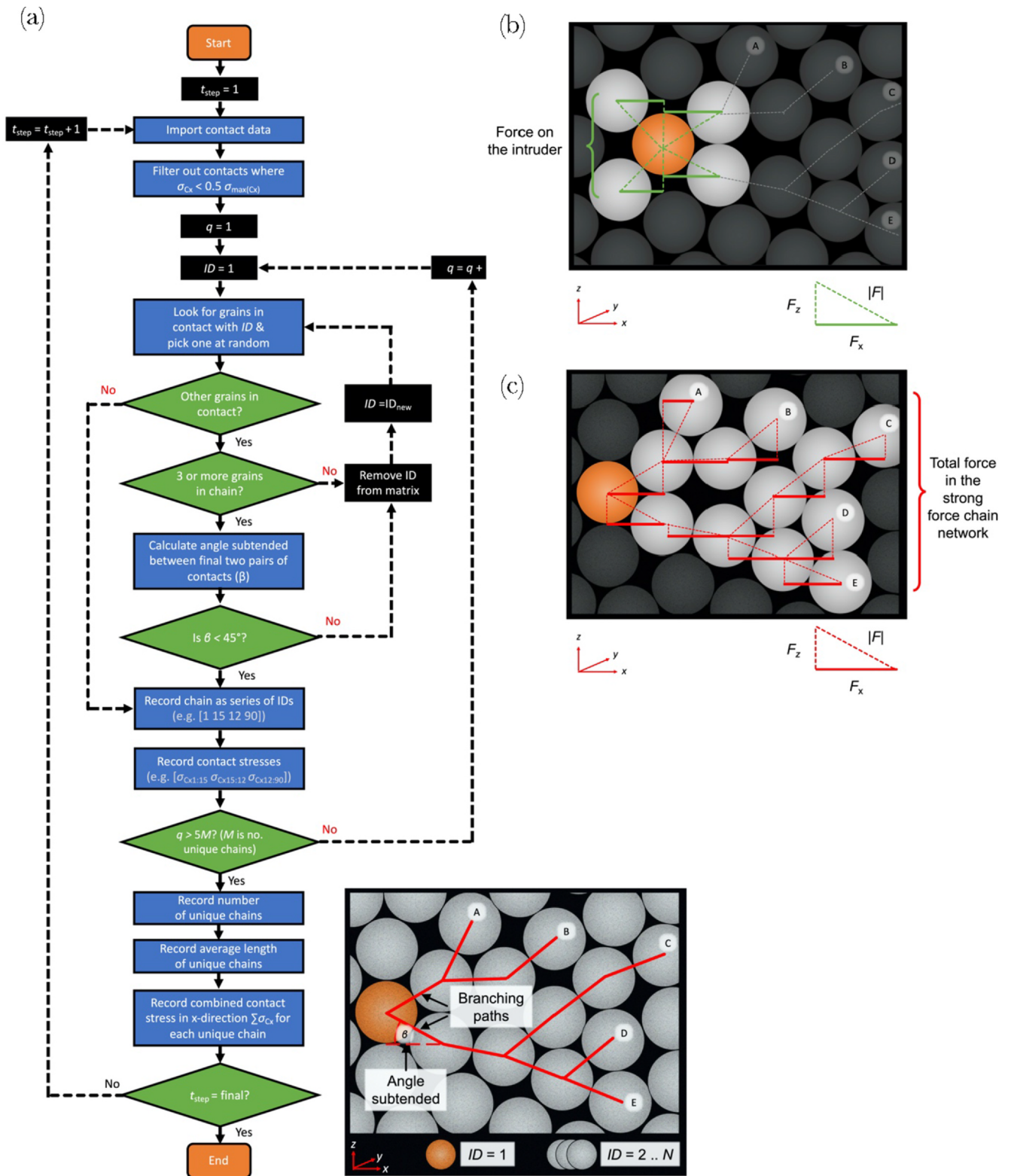


Fig. 4. (a) Flowchart of algorithm for determining properties of the force chain network. The insert schematic shows the types of path that are recorded by the algorithm (A to E), red lines indicate major force chains, whilst minor ones are not shown. The grain intruder is in orange. (b) schematic of the grains participating in the total force on the intruder; (c) schematic of the grains in the strong force chain network. For both (b) and (c), the x-components of the contact forces are summed.

“short” chains comprised three to five contacts, as defined by Tordesillas et al. (2014). The “long” chains comprised six or more contacts. In this study, the bulk granular system was dense, which favoured shorter chains (Muthuswamy & Tordesillas 2006). Long chains are generally considered to be less stable than short chains.

In the case of Fig. 6c(i), where the slip-stick behaviour was most apparent, there were spikes in the number of short force chains during the slippage. This behaviour is consistent with the observations of Tordesillas et al. (2014). The number of long chains did not appear to vary significantly with respect to the stick-slip, implying that on

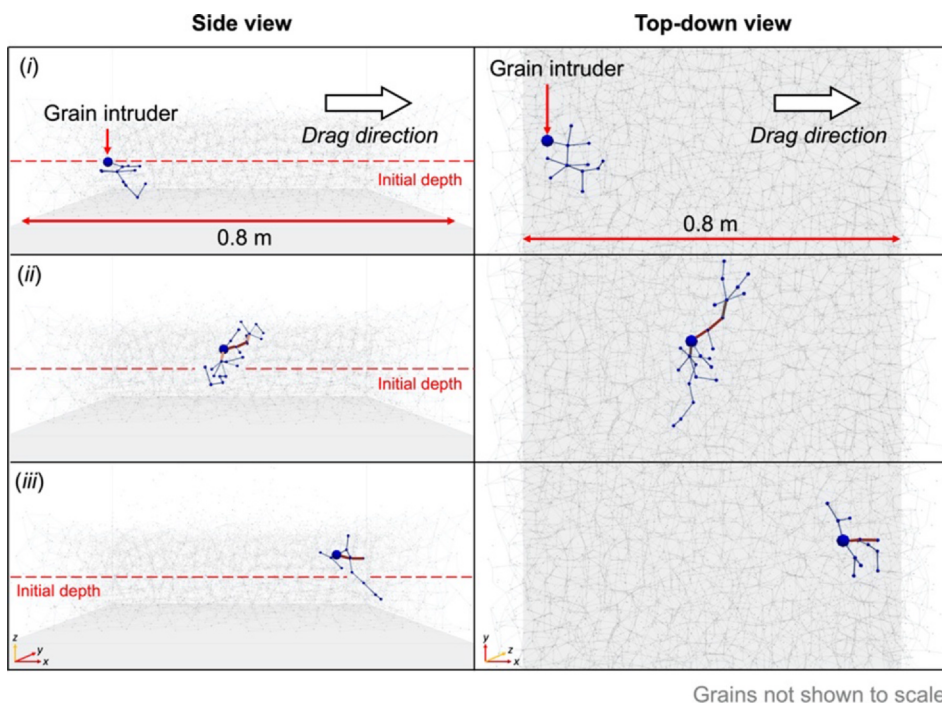


Fig. 5. Side-view of the movement of the grain intruder across the computational domain for input parameters  $k = 1$  kN/m and  $v_{\text{drag}} = 8$  m/s at (i)  $t = 0.0$  s, (ii)  $t = 0.22$  s and (iii)  $t = 0.26$  s. Major force chains that were calculated using the algorithm shown in Fig. 2 are also shown. The colour of the force chains denotes contact force. dark blue is near-zero, whilst red is 1 kN.

average, it was primarily shorter chains that were created and destroyed during the motion. Fig. 6c(ii) is generally similar. However, the large peaks in the number of short chains are absent, because the intruder was almost constantly in motion. Additionally, the population of long chains was slightly smaller than that in Fig. 6c(i) (for the more flexible spring). In Fig. 6c(iii), there is a large initial spike in the number of short chains. The number did not return to the initial value once the intruder started moving.

In summary, the response of the intruder and the bulk assembly strongly depends on both the drag rate and the spring stiffness. Springs that are more flexible prolong the time required for the intruder to traverse the domain and cause far longer sticks between slips. The force on the grain intruder is primarily due to collisions with grains in the bulk assembly, rather than a reaction force to tension mobilised in the spring. The reaction force is transferred to the granular assembly regardless of the drag rate and the spring stiffness. The stick-slip behaviour is difficult to discern for stiff springs and high drag rates, where the bulk granular assembly fluidises.

#### 4.2. Froude number and solid volume fraction

Fig. 7a shows the effects of the drag rate and the spring stiffness on the Froude number  $Fr$ , which is a governing parameter for flow-obstacle interactions (Hilton & Tordesillas, 2013; Armanini et al., 2014; Armanini, 2015; Choi et al., 2015; Faug, 2015).  $Fr$  is given as follows:

$$Fr = \frac{v}{\sqrt{gh}}. \quad (6)$$

We interpret the parameter  $Fr$  in Eq. (6) as a grain Froude number; thus,  $v$  represents the velocity of the grain intruder,  $g$  represents gravitational acceleration, and  $h$  represents the depth of the intruder below the surface of the flow. The grain Froude number is the ratio of the inertia of the grain to the overburden acting on the grain. The data for  $Fr$  shown in Fig. 7a was sampled from a measurement region that moved with the grain intruder (Fig. 2b). The computed values were averaged for the grain intruder as it moved from an  $x$ -position of  $4\delta$  to  $18\delta$ . The data sampling was not started at the origin of the grain intruder ( $x = 2\delta$ ), to prevent an initial build-up of tension in the spring. This is because the time taken for movement to start varied for different

simulation cases. It depended on both the spring stiffness and the drag rate.

The  $Fr$  for the grain intruder increased with the drag rate of the spring for all the spring stiffnesses. The  $Fr$  was maximized for the spring stiffness of  $k = 100$  kN/m. This is because there was almost no extension of the spring; thus, the grain intruder moved at the fixed speed imposed on the spring tether point (see also Fig. 2b). In contrast, for lower spring stiffnesses, the spring underwent significant extension before the grain intruder started to move. Furthermore, after the grain intruder started to move, the spring remained extended. This is why both the average velocity and the  $Fr$  were lower for lower values of  $k$ . Lower values of  $k$  were also correlated with a more prominent increase in the stick-slip behaviour, as shown in Fig. 6a. Notably, for low drag rates ( $v_{\text{drag}} \leq 1$  m/s), the  $Fr$  did not depend strongly on  $k$ . In contrast, for drag rates of  $> 1$  m/s, the  $Fr$  depended strongly on the spring stiffness. At low drag rates, the intruder matched the imposed drag rate. At high drag rates, intruders with low spring stiffnesses ( $k$ ) were unable to accelerate to the rate imposed on the tether point of the spring within the confines of the computational domain.

Fig. 7b shows the mean solid volume fraction in the region surrounding the grain intruder with respect to the drag rate. The region is defined graphically in Fig. 2b as a box with both sides having a length of 6 grain diameters (i.e.  $6\delta$ ) and a height extending from  $3\delta$  above the centroid of the intruder to the base. The initial solid volume fraction was 0.65. For a low drag rate ( $v_{\text{drag}} \leq 2$  m/s), the mean solid volume fraction was approximately 0.6 for each spring stiffness. The grains in the bulk assembly came to rest quickly relative to the total simulation time. As the grain Froude number increased, the mean solid volume fraction tended to decrease. This is because when inertial forces dominated the movement of the grain intruder (Eq. (6)), grains in the bulk assembly came to rest slowly relative to the intruder velocity. As the  $Fr$  increased beyond 5, the solid volume fraction decreased. This is because the velocity of assembly grains moving in response to the grain intruder was slow relative to the intruder velocity.

There were three regimes for the evolution of the solid volume fraction. These regimes depended on (i) the intruder velocity; (ii) the speed at which bulk assembly grains moved in response to the intruder; and (iii) the speed at which bulk assembly grains came to rest. The three aforementioned factors were governed by  $Fr$ , which depended primarily

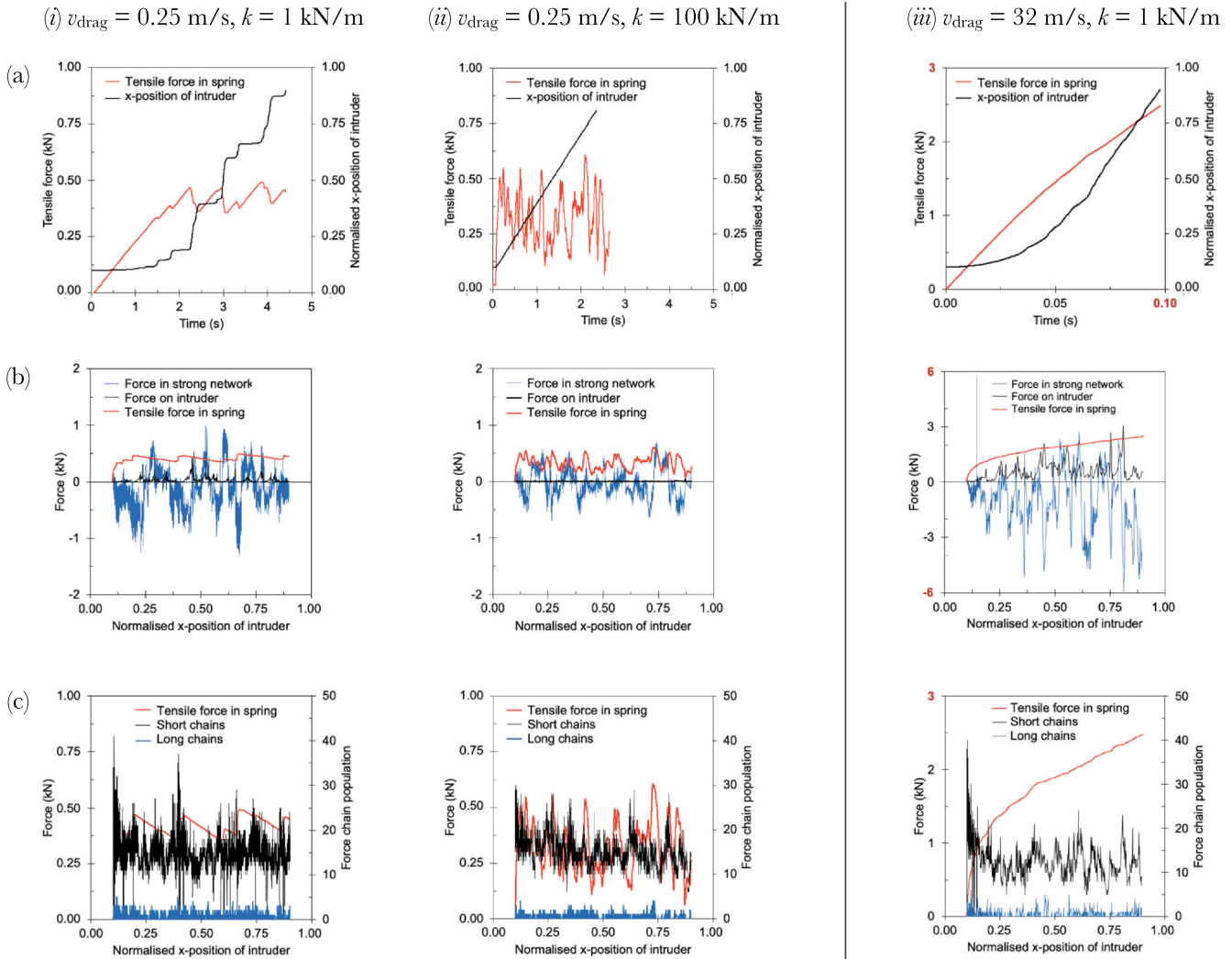


Fig. 6. Effects of drag rate  $v_{drag}$  and spring stiffness  $k$  on (a) tension in the spring & intruder position, (b) force on the intruder and force in the strong force chain network, and (c) the population of short and long force chains. Note. axes for columns (i) and (ii) are scaled differently to column (iii).

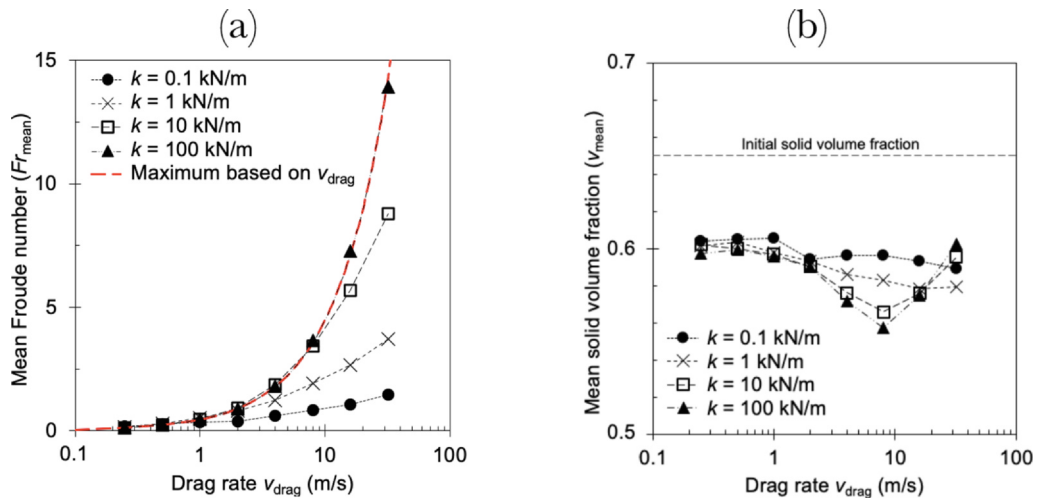


Fig. 7. (a) Mean Froude number and (b) mean solid volume fraction.

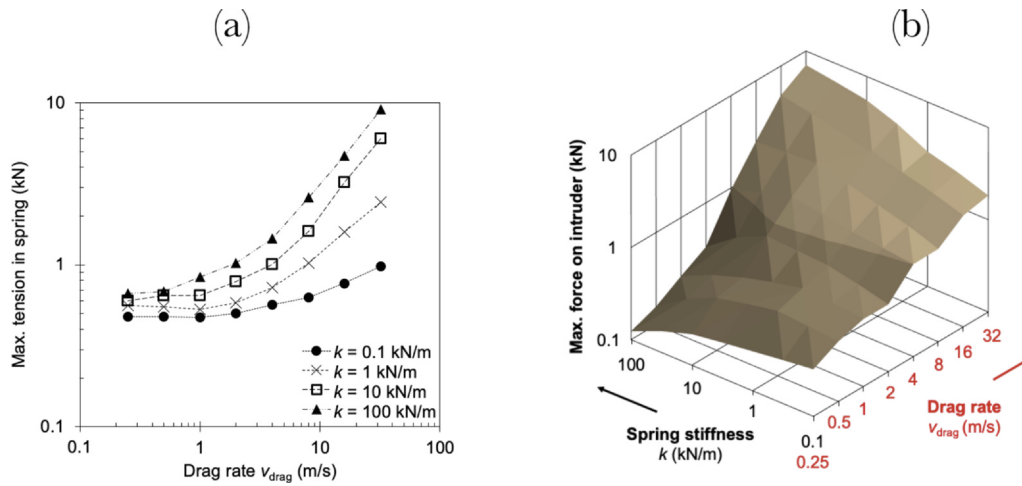


Fig. 8. (a) Maximum tension in the spring and (b) maximum force on the intruder.

on the drag rate, rather than the spring stiffness.

4.3. Maximum spring tension and forces on grain intruder

Two key considerations in the design of flexible countermeasures against geophysical flows are (i) the anticipated tension mobilised in the countermeasure and (ii) the force borne by the countermeasure (see Ng et al. 2016, 2017). Fig. 8(a) shows the relationships between the maximum tension in the spring, the drag rate and spring stiffness. Increasing the drag rate increased the maximum mobilised tension, because the acceleration of the grain intruder was limited by the presence of the granular assembly. This is because the spring tended to extend further when the drag rate was higher, increasing the mobilised tension. Interestingly, increasing the spring stiffness  $k$  also increased the maximum tension mobilised. This is because the rate of loading on the grain intruder was higher for higher values of  $k$ ; thus, the mobilised tension tended to exceed the minimum value needed for movement.

Fig. 8(b) shows the relationships between the maximum force on the intruder, the spring stiffness, and the drag rate of the spring. An increase in the drag rate increased the peak force on the grain intruder. However, as  $k$  increased from 0.1 to 100 kN/m, the range of forces acting on the intruder increased. For low velocities ( $v_{drag} = 0.25$  m/s), the force was strongest for  $k = 0.1$  kN/m. For high velocities ( $v_{drag} = 32$  m/s), the force was weakest for  $k = 0.1$  kN/m. The increase in the force was linear. For stiffer springs ( $k = 100$  kN/m), the forces on the grain intruder were almost an order of magnitude stronger.

The nonlinear behaviour for different drag rates and spring stiffnesses was due to the following two competing mechanisms.

In the first mechanism, the tension  $T$  in the spring decreased owing to contraction when the intruder slipped, according to  $T = kx$ . The extent to which the tension decreased ( $\Delta T$ ) for a given slip distance ( $x$ ) was inversely proportional to the spring stiffness ( $k$ ). If  $k$  was low, the rate at which the tension decreased during the slippage was low. Thus, the force exerted on the grain intruder was relatively uniform during the slippage, as shown in Fig. 6b(i). For low values of  $k$  and low drag rates, the force acting on the intruder was sustained to a greater degree. The flexible springs generated a relatively strong impact force when the intruder impacted the grains in the bulk assembly.

The second mechanism was observed at higher drag rates. The peak impact force was higher for stiffer obstacles. For low values of  $k$ , the intruder lagged far behind the tether point of the spring. The impact force on the intruder was reduced because the velocity was lower, causing a lower impact force (Eq. (2)).

This again implies that more flexible obstacles may be more robust: the velocity of an incoming flow may be unpredictable; thus, using more flexible obstacles helps to narrow the range of forces to which the obstacles may be subjected.

4.4. Work done on granular assembly

In a grain-intruder setup, the energy input into the system comes from the extension of the spring attached to the grain intruder. This

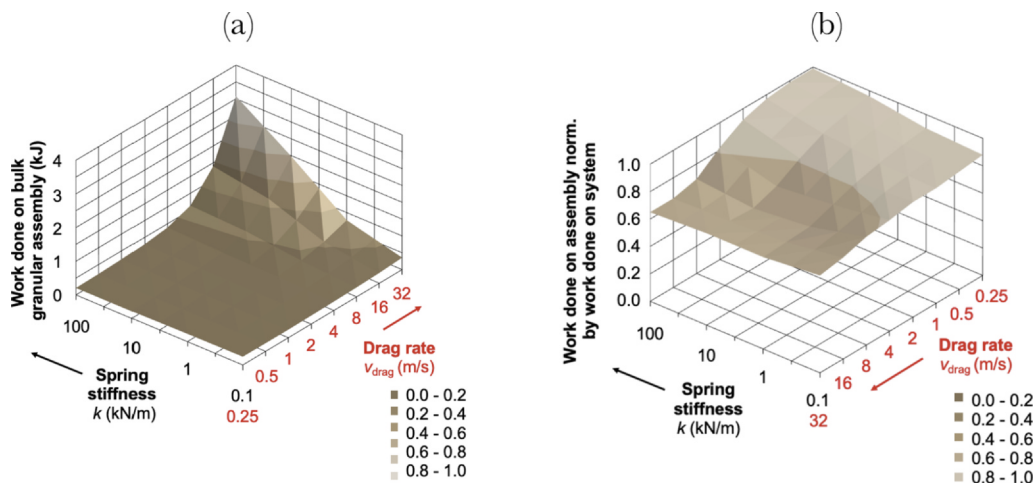


Fig. 9. (a) Work done on granular assembly; (b) work done on the assembly normalized by that done on the system (i.e. including the grain intruder).

energy increases when the grain intruder becomes stuck and is released into the rest of the system each time the grain intruder slips. However, it is unclear how the transfer of energy from the virtual spring to the system is apportioned between the grain intruder and the bulk assembly of grains. For landslide mitigation, energy transfer to the bulk granular assembly rather than the obstacle is ideal. This is because internal shearing from the bulk assembly can be used to dissipate energy (Ng et al., 2017), and the chances of the obstacle being damaged are reduced.

Because the system is initially static, the energy dissipation by the bulk granular assembly is equivalent to the work done on the bulk granular assembly, which can be calculated as follows:

$$W_{\text{bulk}} = W_{\text{spring}} - W_{\text{intruder}} = \int kx dx - \int F dx. \quad (7)$$

As shown in Fig. 9a, the work done on the granular assembly remained approximately constant for different spring stiffnesses for drag velocities of  $\leq 1$  m/s. For drag velocities of  $\geq 2$  m/s, the work done on the granular assembly started to increase and diverged for different stiffnesses. This divergence was due to the changes in  $F_r$ , which are shown in Fig. 7a. More flexible obstacles were clearly less able to cause energy to be dissipated within the granular assembly than stiffer ones. This is because flexible springs allowed the grain intruder to take the path of least resistance, reducing the amounts of shearing and collisions in the bulk granular assembly. This suggests that rigid obstacles are more desirable for causing energy dissipation, in contrast to the hypothesis of Ng et al. (2016). However, the energy dissipation was enhanced at the cost of additional force being exerted on the obstacle (Fig. 8b).

Fig. 9b shows the work done on the bulk assembly normalised by the total work done on the system. If the normalised work is zero, all the work is done on the grain intruder; conversely, a normalised work of unity indicates that all the work is done on the granular assembly. The normalised energy dissipation was relatively uniform across the range of spring stiffnesses and drag rates investigated, with an average value of approximately 80% of the work done on the granular assembly. The energy-dissipation efficiency of the granular assembly was inversely proportional to the drag rate. For example, for  $k = 100$  kN/m, the work done on the assembly was almost 100% at a drag rate of 0.25 m/s but slightly higher than 60% at a drag rate of 32 m/s. The range of energy dissipation was reduced from  $\sim 40\%$  for the stiffest spring to  $\sim 20\%$  for a spring stiffness of  $k = 0.1$  kN/m. This confirms the cost of using a rigid obstacle, with regard to both the (i) force and (ii) work done on it.

The results in Fig. 9 seem to concur with results from other studies on flexible barriers that indicate that the current engineering state-of-the-art may be overconservative. Indeed, GEO (2014) recommend that a factor of safety should be applied to the energy rating for flexible barriers. This recommendation contrasts with results from other studies. Huo et al. (2017) used a physical flume 6 m long to investigate the energy dissipation for flows impacting a flexible barrier made of chicken wire with a bulk elastic modulus of 0.45 GPa. The authors reported that 64% of the energy was dissipated by the flexible barrier (Song et al., 2019b), implying a reduction factor of 0.64. The results of Cheung et al. (2018), who performed numerical simulations to evaluate the energy dissipated by flexible barriers, suggest reduction factors in the range of 0.07–0.30. Kwan et al. (2018) used an FEM package capable of modelling large-scale deformation to model simulated flows impacting flexible barriers. Their results indicated that a reduction factor of 0.06 adequately described the energy taken by the flexible barrier. Song et al. (2019a) used a centrifuge to model dry sand flows impacting an impervious flexible barrier. The cable stiffness was 142 kN/m. The authors reported that the barrier had an equivalent energy rating of 1000 kJ. The impact energy was reported to be 1200 kJ, and the energy absorbed by the barrier was 100 kJ, corresponding to a reduction factor of approximately 0.08.

Clearly, the range of reduction factors for flexible barriers is wide: 0.08–0.64. The results of the grain-intruder tests in this study fall within this range, with equivalent reduction factors ranging from almost zero for slow flows and stiff obstacles to just under 0.4 for faster flows (32 m/s). The differences may be due to the grain-intruder setup allowing grains to flow past the obstacle whilst not capturing the effects of the formation of a dead zone (Song et al., 2019a) (which itself may both shield the barrier and enable energy dissipation through shearing). Nonetheless, the results of this study demonstrate for the first time that the granular assembly can dissipate a majority of the flow energy due to shearing during interaction with a simple obstacle, which is separate from the energy dissipation that occurs during the flow. The apportionment of the energy dissipation was unclear in previous studies (e.g. Huo et al., 2017; Cheung et al., 2018; Song et al., 2019a).

## 5. Conclusions

Experimental data from a physical grain-intruder setup were used to calibrate a discrete element model (DEM) to investigate the fundamental behaviour of flexible obstacles used to resist granular flows. The calibrated DEM was used to conduct a parametric study to examine a wide range of obstacle stiffnesses and loading rates. The following conclusions are drawn:

1. The response of the intruder and the bulk assembly depends heavily on both the drag rate and the intruder stiffness. Stick-slip behaviour is difficult to discern for stiffer obstacles and high drag rates ( $> 1$  m/s), where the bulk granular assembly fluidises. Furthermore, the peak loads experienced by a softer obstacle experiences lower maximum and minimum values.
2. The force experienced by the intruder is primarily due to contact and collisional grain stresses induced by the granular assembly rather than the applied tensile force. Softer obstacles prolong the time required for the intruder to traverse the domain and cause significantly longer sticks between slips. At least 60% of the work is transferred from the intruder to the granular assembly regardless of the drag rate and obstacle stiffness.
3. The results of this study suggest that rigid obstacles are more desirable for causing energy dissipation by the granular assembly, while flexible obstacles are more desirable for reducing the resisting forces required.

## CRedit authorship contribution statement

**C.E. Choi:** Conceptualization, Methodology, Software, Validation, Formal analysis, Investigation, Data curation, Writing - original draft, Writing - review & editing. **G.R. Goodwin:** Conceptualization, Methodology, Resources, Writing - original draft, Writing - review & editing, Supervision, Project administration, Funding acquisition.

## Declaration of Competing Interest

The authors declare that they have no known competing financial interests or personal relationships that could have appeared to influence the work reported in this paper.

## Acknowledgements

The authors are thankful for the funding from the National Natural Science Foundation of China (NNSFC) (51709052), as well as the Research Grants Council of Hong Kong (General Research Fund Grant 16210219, 16209717 and 16212618, Area of Excellence grant AoE/E-603/18 and Theme-based Research grant: T22-603/15N). Editing services from Elsevier were financed via the NNSFC grant.

## References

- Albaba, A., Lambert, S., Kneib, F., Chareyre, B., Nicot, F., 2017. DEM modeling of a flexible barrier impacted by a dry granular flow. *Rock Mech. Rock Eng.* 50 (11), 3029–3048.
- Albaba, A., Lambert, S., Faug, T., 2018. Dry granular avalanche impact force on a rigid wall: analytic shock solution versus discrete element simulations. *Phys. Rev. E* 97 (052903), 1–12.
- Albert, R., Pfeifer, M.A., Barabási, A.-L., Schiffer, P., 1999. Slow drag in a granular medium. *Phys. Rev. Lett.* 82 (1), 205–208.
- Albert, I., Tegzes, P., Kahng, B., Albert, R., Sample, J.G., Pfeifer, M., Barabási, A.L., Vicsek, T., Schiffer, P., 2000. Jamming and fluctuations in granular drag. *Phys. Rev. Lett.* 84, 5122.
- Albert, I., Tegzes, P., Albert, R., Sample, J.G., Barabási, A.L., Vicsek, T., Kahng, B., Schiffer, P., 2001. Stick-slip fluctuations in granular drag. *Phys. Rev. E* 64, 031307.
- Armanini, A., Larcher, M., Nucci, E., Dumbser, M., 2014. Submerged granular channel flows driven by gravity. *Adv. Water Resour.* 63, 1–10.
- Armanini, A., 2015. Closure relations for mobile bed flows in a wide range of slopes and concentrations. *Adv. Water Resour.* 81, 75–83.
- Ashwood, W., Hungri, O., 2016. Estimating total resisting force in flexible barrier impacted by a granular avalanche using physical and numerical modelling. *Can. Geotech. J.* 53 (10), 1700–1717.
- Brighenti, R., Segalini, A., Ferrero, A.M., 2013. Debris flow hazard mitigation: a simplified analytical model for the design of flexible barriers. *Comput. Geotech.* 54, 1–15.
- Candelier, R., Dauchot, O., 2009. Creep motion of an intruder within a granular glass close to jamming. *Phys. Rev. Lett.* 103, 128001.
- Candelier, R., Dauchot, O., 2010. Journey of an intruder through the fluidization and jamming transitions of a dense granular media. *Phys. Rev. E* 81 (1), 100304.
- Canelli, L., Ferrero, A.M., Migliazza, M., Segalini, A., 2012. Debris flow risk mitigation by the means of rigid and flexible barriers – experimental tests and impact analysis. *Nat. Hazards Earth Syst. Sci.* 12, 1693–1699.
- Cates, M.E., Wittmer, J.P., Bouchaud, J.-P., Claudin, P., 1998. Jamming, force chains and fragile matter. *Phys. Rev. Lett.* 81 (9–31), 1841–1845.
- Ceccato, F., Redaelli, L., di Prisco, C., Simonini, P., 2018. Impact forces of granular flows on rigid structures: comparison between discontinuous (DEM) and continuous (MPM) numerical approaches. *Comput. Geotech.* 103, 201–217.
- Cheung, A.K., Yiu, J., Lam, H.W., Sze, E.H., 2018. Advanced numerical analysis of landslide debris mobility and barrier interaction. *HKIE Transactions* 25 (2), 76–89.
- Choi, C.E., Au-Yeung, S.C.H., Ng, C.W.W., Song, D., 2015. Flume investigation of landslide granular debris and water runoff mechanisms. *Géotechnique Lett.* 5 (1), 28–30.
- Ding, Y., Gravish, N., Goldman, D.L., 2011. Drag induced lift in granular media. *Phys. Rev. Lett.* 106 (2), 028001.
- Faug, T., Lachamp, P., Naaim, M., 2002. Experimental investigation on steady granular flows interacting with an obstacle down an inclined channel: study of the dead zone upstream from the obstacle. Application to interaction between dense snow avalanches and defense structures. *Nat. Hazards Earth Syst. Sci.* 2, 187–191.
- Faug, T., Beguin, R., Benoit, C., 2009. Mean steady granular force on a wall over-flowed by free-surface gravity-driven dense flows. *Phys. Rev. E* 80, 201305.
- Faug, T., 2015. Macroscopic force experienced by extended objects in granular flows over a very broad Froude-number range. *Eur. Phys. J. E* 38 (5), 120. <https://doi.org/10.1140/epje/i2015-15034-3>.
- Geng, J., Behringer, R.P., 2005. Slow drag in two-dimensional granular media. *Phys. Rev. E* 71 (1), 011302.
- GEO (Geotechnical Engineering Office) (2014). GEO Technical Guidance Note No. 37: Guidelines on empirical design of flexible barriers for mitigating natural terrain open hillslope landslide hazards. Geotechnical Engineering Office, Civil Engineering and Development Department. The Government of the Hong Kong Special Administrative Region, People's Republic of China.
- Goodwin, G.R., Choi, C.E., 2020. Slit structures: fundamental mechanisms of mechanical trapping of granular flows. *Comput. Geotech.* 199, 103376.
- Harich, R., Darnige, T., Kolb, E., 2011. Intruder mobility in a vibrated granular packing. *Europhys. Lett.* 96, 54003.
- Hilton, J.E., Tordesillas, A., 2013. Drag force on a spherical intruder in a granular bed at low Froude number. *Phys. Rev. E* 88, 062203.
- Huo, M., Zhou, J.W., Yang, X.G., Zhou, H.W., 2017. Effects of a flexible net barrier on the dynamic behaviours and interception of debris flows in mountainous areas. *J. Mount. Sci.* 14, 1903–1918.
- Iverson, R.M., 1997. The physics of debris flows. *Rev. Geophys.* 35, 245–296.
- Johnson, P.A., Savage, H., Knuth, M., Gombert, J., Marone, C., 2008. Effects of acoustic waves on stick-slip in granular media and implications for earthquakes. *Nature* 451, 57–60.
- Kloss, C., Goniva, C., 2011. LIGGGHTS – a new open source discrete element simulation software. In: Proceedings of the 5th International Conference on Discrete Element Methods 2011, p. 25–26.
- Kolb, E., Cixous, P., Gaudouen, N., Darnige, T., 2013. Rigid intruder inside a two-dimensional dense granular flow: drag force and cavity formation. *Phys. Rev. E* 87 (3), 032207.
- Koo, R.C.H., Kwan, J.S.H., Lam, C., Ng, C.W.W., Yiu, J., Choi, C.E., Ng, A.K.L., Ho, K.K.S., Pun, W.K., 2016. Dynamic response of flexible rockfall barriers under different loading geometries. *Landslides* 14 (3), 905–916.
- Kwan, J.S., Sze, E.H.Y., Lam, C., 2018. Finite element analysis for rockfall and debris flow mitigation works. *Can. Geotech. J.* 56 (9), 1225–1250. <https://doi.org/10.1139/cgj-2017-0628>.
- Lee, K., Kim, Y., Ko, J., Jeong, S., 2019. A study on the debris flow-induced impact force on check dam with- and without-entrainment. *Comput. Geotech.* 113, 103104.
- Leonardi, A., Wittle, F.K., Mendoza, M., Vetter, R., Herrmann, H.J., 2016. Particle-fluid-structure interaction for debris flow impact on flexible barriers. *Comput.-Aided Civ. Infrastruct. Eng.* 31 (5), 323–333.
- Leonardi, A., Pirulli, M., 2020. Analysis of the load exerted by debris flows on filter barriers: comparison between numerical results and field measurements. *Comput. Geotech.* 118, 103311.
- Majmudar, T.S., Behringer, R.P., 2005. Contact force measurements and stress-induced anisotropy in granular materials. *Nature* 435, 1079–1082.
- Makse, H.A., Johnson, D.L., Schwartz, L.M., 2000. Packing of compressible granular materials. *Phys. Rev. Lett.* 84 (18), 4160–4163.
- Marchelli, M., Leonardi, A., Pirulli, M., Scavia, C., 2019. On the efficiency of slit-check dams in retaining granular flows. *Géotechnique* 70 (3), 226–237. <https://doi.org/10.1680/jgeot.18.p.044>.
- Mitarai, N., Nakanishi, H., 2007. Velocity correlations in dense granular shear flows: effects on energy dissipation and normal stress. *Phys. Rev. E* 75, 031305.
- Moriguchi, S., Borja, R.I., Yashima, A., Sawada, K., 2009. Estimating the impact force generated by granular flow on a rigid obstruction. *Acta Geotech.* 4 (1), 57–71.
- Muthuswamy, M., Tordesillas, A., 2006. How do interparticle contact friction, packing density and degree of polydispersity affect force propagation in particulate assemblies? *J. Stat. Mech: Theory Exp.* P09003. <https://doi.org/10.1088/1742-5468/2006/09/P09003>.
- Ng, C.W.W., Song, D., Choi, C.E., Koo, R.C.H., Kwan, J.S.H., 2016. A novel flexible barrier for landslide impact in centrifuge. *Géotechnique Lett.* 6 (3), 221–225.
- Ng, C.W.W., Song, D., Choi, C.E., Liu, H.D., Kwan, J.S.H., Koo, C.H., Pun, W.K., 2017. Impact mechanisms of granular and viscous flows on rigid and flexible barriers. *Can. Geotech. J.* 54 (2), 188–206.
- Ng, C.W.W., Choi, C.E., Goodwin, G.R., 2019. Froude characterisation for single-surge unsteady dry granular flows: impact pressure and runoff height. *Can. Geotech. J.* 56 (12), 1968–1978. <https://doi.org/10.1139/cgj-2018-0529>.
- Peters, J.F., Muthuswamy, M., Wibowo, J., Tordesillas, A., 2005. Characterisation of force chains in granular material. *Phys. Rev. E* 72, 041307.
- Rickenmann, D., 1999. Empirical relationships for debris flows. *Nat. Hazards* 19, 47–77.
- Sano, T.G., Hayakawa, H., 2012. Simulation of granular jets: is granular flow really a perfect fluid? *Phys. Rev. E* 86, 041308.
- Song, D., Zhou, G.G.D., Xu, M., Choi, C.E., Li, S., Zheng, Y., 2019a. Quantitative analysis of debris-flow flexible barrier capacity from momentum and energy perspectives. *Eng. Geol.* 251, 8–92.
- Song, D., Zhou, G.G.D., Choi, C.E., Zheng, Y., 2019b. Debris flow impact on flexible barrier: effects of debris-barrier stiffness and flow aspect ratio. *J. Mount. Sci.* 16 (7), 1629–1645.
- Teufelsbauer, H., Wang, Y., Pudasaini, S.P., Borja, R.I., Wu, W., 2011. DEM simulation of impact force exerted by granular flow on rigid structures. *Acta Geotech.* 6, 119–133.
- Tordesillas, A., 2007. Force chain buckling, unjamming transitions and shear banding in dense granular assemblies. *Phil. Mag.* 87 (32), 2987–5016.
- Tordesillas, A., Muthuswamy, M., 2009. On the modeling of confined buckling of force chains. *J. Mech. Phys. Solids* 57, 706–727.
- Tordesillas, A., Zhang, J., Behringer, R., 2009. Buckling force chains in dense granular assemblies: physical and numerical experiments. *Geomech. Geoenviron. Eng.* 4 (1), 3–16.
- Tordesillas, A., Walker, D.M., Lin, Q., 2010. Force cycles and force chains. *Phys. Rev. E* 81, 011302.
- Tordesillas, A., Hilton, J.E., Tobin, S.T., 2014. Stick-slip and force chain evolution in a granular bed in response to a grain intruder. *Phys. Rev. E* 89, 042207.
- Walker, D.M., Tordesillas, A., Kuhn, M.R., 2017. Spatial connectivity of force chains in a simple shear 3D simulation exhibiting shear bands. *J. Eng. Mech.* 143 (1), C4016009.
- Wendeler, C., Volkwein, A., Roth, A., Denk, M. & Wartmann, S. (2007). Field measurements and numerical modelling of flexible debris flow barriers. In: Proceedings of Debris-Flow Hazards Mitigation: Mechanics, Prediction, and Assessment, Davos, Switzerland, 10–12 September 2007.